# Facile General Route toward Tunable Magnéli Nanostructures and Their Use As Thermoelectric Metal Oxide/Carbon Nanocomposites

David Portehault,[†,‡,§,*] Vasana Maneeratana,[⊥] Christophe Candolfi,[‖] Niels Oeschler,[‖] Igor Veremchuk,[‖] Yuri Grin,[‖] Clément Sanchez,[†,‡,§] and Markus Antonietti[⊥]

[†]UPMC Univ Paris 06, UMR 7574, Chimie de la Matière Condensée de Paris, Collège de France, 11 place Marcelin Berthelot, 75231 Paris Cedex 05, France, [‡]CNRS, UMR 7574, Chimie de la Matière Condensée de Paris, Collège de France, F-75005 Paris, France, [§]Collège de France, Chimie de la Matière Condensée de Paris, Collège de France, F-75005 Paris, France, [⊥]Department of Colloid Chemistry, Max-Planck-Institute of Colloids and Interfaces, Research Campus Golm, 14424 Potsdam, Germany, and [‖]Max-Planck-Institut für Chemische Physik fester Stoffe, Dresden 01187, Germany

Recently, a long known family of titanium oxides, namely, $Ti_nO_{2n-1}$ ($4 \leq n \leq 9$) phases, has experienced a strong revival due to its surprising and unexpected electronic and phononic properties. During the last few months, metal $Ti_4O_7$ nanofilaments were evidenced to play a major role in $TiO_2$ resistive switching memory,[1] while light-triggered metal−semiconductor transition was demonstrated for $Ti_3O_5$.[2] Different bulk $Ti_nO_{2n-1}$ phases ($n = 4, 5, 6, 8, 9$) were also recently reported as efficient thermoelectric materials within the oxide family.[3] These three examples show the potential of these ordered substoichiometric titanium oxides for the design of novel information storage and energy conversion devices. Magnéli was the first to solve the structure of these compounds in the 1950s,[4−7] which is closely related to the single strings of edge-sharing $TiO_6$ octahedra observed in rutile $TiO_2$, except that shearing occurs every $n$th octahedra (Figure 1), as a consequence of partial reduction of titanium(IV) to titanium(III) and the resulting oxygen vacancies.[8−11] For thermoelectricity, these crystallographic shear planes can act as phonon-scattering centers,[3] thus reducing the thermal conductivity while maintaining a high electron mobility and large thermopower.[3] Moreover, the reduction degree (increasing as $n$ decreases) allows fine adjustment of the electrical properties, providing either semiconductor ($Ti_5O_9$ and $Ti_6O_{11}$) or metallic ($Ti_4O_7$) behavior at room temperature.[12,13] Because of these remarkable bulk properties,[14,15] some of these compounds, mostly

**ABSTRACT** Engineering nanoscale interfaces is a requisite for harnessing electrical and thermal transports within nanostructured materials, especially those destined for thermoelectric applications requiring an unusual combination of low thermal conductivity and electrical resistivity. Nanocomposites open up possibilities in this area, but are still bound to a very narrow range of materials. Here, we report a new approach combining the sol−gel process toward hybrid materials with spark plasma sintering (SPS) to yield functional nanocomposites based on substoichiometric titanium oxides $Ti_nO_{2n-1}$, so-called Magnéli phases. The potential of this new approach is demonstrated by three results. First, multiple $Ti_nO_{2n-1}$ compounds ($n = 3, 4, 5, 6, 8$) are obtained for the first time as sole nano-Magnéli crystalline phases with controlled specific surface areas from 55 to 300 $m^2 \cdot g^{-1}$, classified as potential thermoelectric n-type metal oxides and paving the way toward advanced systems for energy-harvesting devices and optoelectronics. Second, this work combines the use of sol−gel and SPS processes to yield percolated nanocomposites based on metal oxide nanoparticles embedded in a carbon matrix with low electrical resistivity ($2 \times 10^{-4}$ $\Omega \cdot m$ for a $Ti_4O_7$ compound) and reduced thermal conductivity ($1$ $W \cdot m^{-1} \cdot K^{-1}$) with respect to bulk phases. Finally, the discovered materials are reliable with thermoelectric figures of merit ($ZT = 0.08$) relatively high for n-type Ti−O-based systems and metal oxides. Thereby this study represents a proof of concept for the development of promising, cheaper, and more efficient thermoelectric conversion devices.

**KEYWORDS:** Magnéli phases · nanocomposites · porous materials · nanoparticles · thermoelectricity

phase mixtures of different $n$, were commercialized in the 1980s under the trademark Ebonex and were mostly used for cathodic protection and as electrode materials and catalyst supports.[13,16−19] Advances in other application fields were mostly hindered by synthetic and processing difficulties, especially in the production of nanoscaled Magnéli phases. In addition, the thermoelectric properties of the bulk materials are still suffering from a relatively high thermal conductivity.[3] A fundamental leap in the direction of efficient thermoelectric
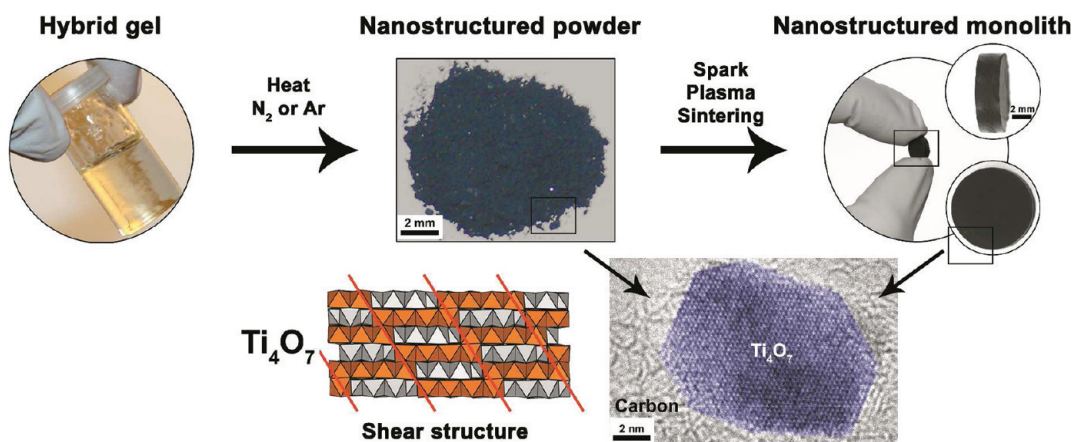
**Figure 1.** Combined sol−gel/spark plasma sintering strategy toward Magnéli/carbon nanocomposites.
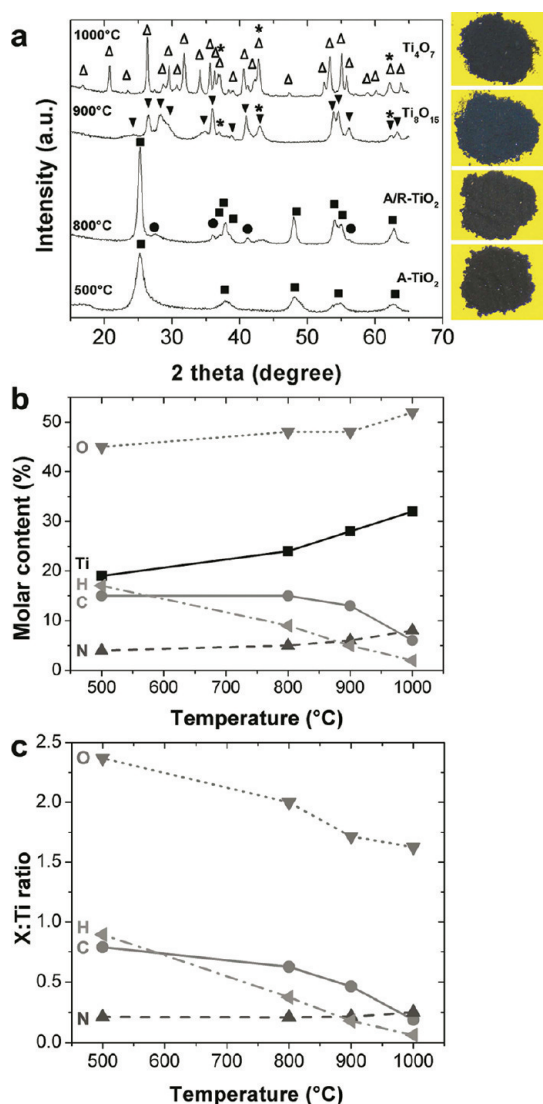


**Figure 2.** (a) XRD patterns of samples obtained from a hybrid gel ethanol:TEOTi:PEI = 2:10:6 wt and calcined under nitrogen at various temperatures. Squares: anatase $TiO_2$, circles: rutile $TiO_2$, inversed triangles: $Ti_8O_{15}$, open triangles: $Ti_4O_7$, stars: TiN. (b) Absolute and (c) relative molar composition of the corresponding calcined samples.

conversion could arise from the nanostructuring of composites and inorganic−organic hybrids with additional phonon scattering at nanoscale interfaces.[20,21]

To address these previous weaknesses, we develop hereafter a general approach for the synthesis of various nanoscaled Magnéli compounds under mild conditions contrasting drastically with typical bulk syntheses in harsh conditions[2,14,22−26] or the rare reports on $Ti_8O_{15}$[27] and $Ti_3O_5$[2] nanoparticles obtained by reduction of $TiO_2$ particles in a highly reductive atmosphere. Furthermore, these materials are processed in order to provide bulk nanostructured monoliths with enhanced thermoelectric behavior.

The conceptual advancement of this new bottom-up approach toward functional nanocomposites (Figure 1) lies in the combination of the sol−gel process, mostly known in oxide materials chemistry for its versatility and scalability, and spark plasma sintering (SPS), typically used in ceramics and alloys fields to sinter while limiting grain growth. Although SPS was already reported for incorporation of carbon nanostructures (nanotubes, nanofilaments) into sol−gel-derived microstructured oxide matrixes,[28] here both components are nanoscaled and originate from a one-pot sol−gel process. This first step yields for the first time single-phase "nano-Magnéli"/carbon nanopowders, while subsequent application of SPS generates Magnéli/carbon nanocomposite monoliths. The thermoelectric efficiency of these monolithic materials is enhanced through reduction of the thermal conductivity, yielding thermoelectric figures of merit relatively high for n-type Ti−O-based materials and more generally n-type metal oxides. This suggests that improved n-type thermoelectric systems based on cheap, air-stable, and environmentally benign metal oxides[29,30] might be further discovered among Magneli/carbon nanocomposites.

## RESULTS AND DISCUSSION

As a result from the sol−gel path, multiple $Ti_nO_{2n-1}$ compounds ($n$ = 3, 4, 5, 6, 8) are obtained as sole

ACSNANO
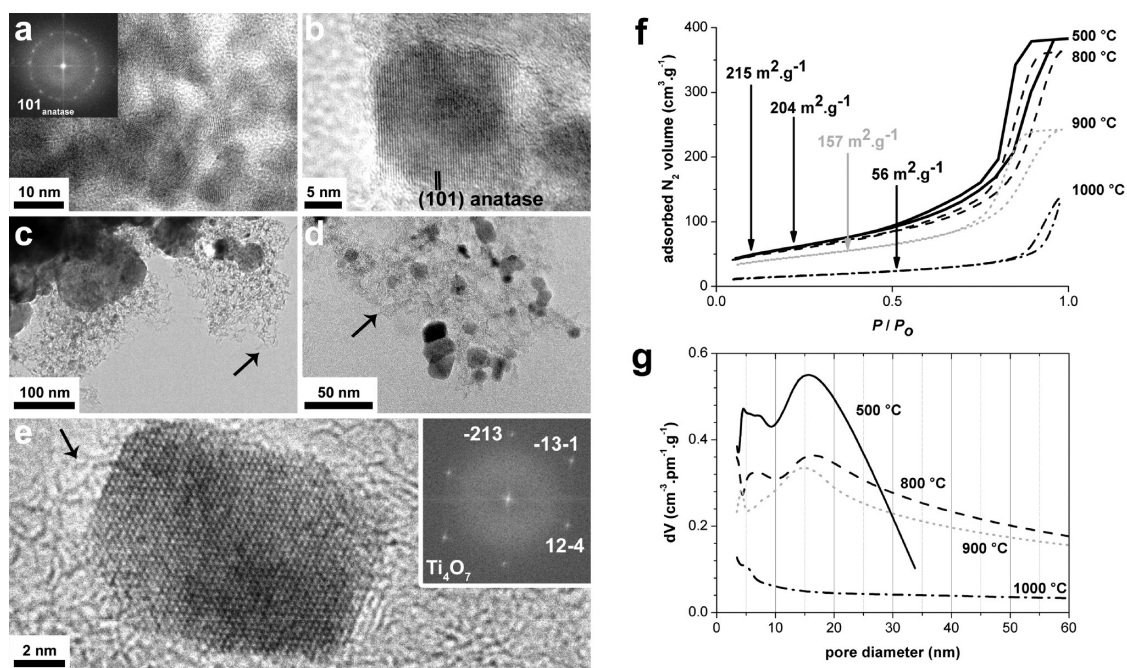
**Figure 3.** (HR)TEM images and corresponding FFT analyses of titania/Magnéli–carbon composites obtained by calcination under nitrogen of a hybrid gel ethanol:TEOTi:PEI = 2:10:6 wt at (a) 500, (b) 800, (c) 900, and (d, e) 1000 °C. Black arrows indicate the carbon matrix. (f) N$_2$ sorption isotherms, $S_{BET}$, and (g) pore size distribution for composites obtained at various temperatures.

nano-Magnéli phases, most of them for the first time, enabling broader use in the fields of energy harnessing, catalysis, and optoelectronics.[1–3,13,16–19] This "one-pot" sol–gel process allows adaptable control of the structural and textural features, as well as the electrical properties of the nanostructured powders, which in principle opens up the toolbox for further optimization of the nanostructure. In this simple, versatile, and scalable sol–gel process, titanium(IV) ethoxide (TEOTi) was mixed with diverse amino- or ethoxy-containing oligomers or polymers such as diethylenetriamine (DETA), polyethylenimine (PEI, inset of Figure S1 in the Supporting Information), or polyethyleneglycol (PEG). The mixture readily turns into homogeneous gels through secondary cross-linking of the organic (macro)molecules. A small amount of ethanol is added to ensure a sufficiently low viscosity for suitable homogenization kinetics. The as-obtained clear gels are calcined at different temperatures under nitrogen or argon, yielding dark blue powders above 900 °C (Figures 1 and 2).

Thermogravimetric analysis (TGA, Figure S1) under nitrogen flow of a PEI-based gel (ethanol:TEOTi:PEI = 2:10:6 wt, $M_n$(PEI) = 25000 g·mol$^{-1}$) exhibits two mass loss steps below 150 °C and at 300 °C, which can be attributed to ethanol loss and the primary decomposition of the organic moieties, respectively. A third mass loss at 600 °C is ascribed to the elimination of multibonded carbon- or nitrogen-containing species. XRD patterns, recorded for samples obtained at different temperatures under nitrogen, highlight the structural

evolution of the titanium-based species (Figure 2a and Table S1). Crystallization occurs above 500 °C, forming pure TiO$_2$ anatase at 500 °C and a mixture of anatase and TiO$_2$ rutile at 800 °C. Further heating leads to an abrupt change of the structure and the formation of crystalline Ti$_8$O$_{15}$ at 900 °C and Ti$_4$O$_7$ at 1000 °C. At these temperatures, the intimately mixed carbon promotes partial carbothermal reduction from Ti(IV) to Ti(III). As a result, the crystalline structure of titanium oxides from stoichiometric TiO$_2$ to various defined Magnéli phases is easily adjusted by controlling the temperature. Careful analysis of the XRD patterns above 900 °C suggests the presence of TiN as a minor phase (Figure 2a), which can be avoided by tuning the synthesis conditions as explained later. The clear high phase selectivity of this synthetic procedure through the calcination temperature, combined with the simplicity of the sol–gel process, greatly contrasts with typical reports on the synthesis of a single Magnéli phase[23,31,32] by using complex procedures such as solid-state reaction between Ti and TiO$_2$,[5,14] chemical vapor transport,[23,24] or reaction of TiO$_2$ with a reactive atmosphere,[14,16] involving high temperature, low pressure, and/or highly reductive atmospheres.[5,16,24,25,31,33]

Elemental analysis supports the interpretation of the ongoing transformation processes. Below 800 °C, Ti, O, C, and N contents only slightly change (Figure 2b,c and Table S2). The O:Ti ratio of 2.3 at 500 °C accounts for residual oxygenated species from incomplete decomposition of the polymer. At 800 °C, O:Ti ≈ 2.0 confirms the identification of TiO$_2$ crystalline phases from XRD

with complete carbonization of the organic component, while the carbon content of 20 mol % supports the existence of a second, disordered, carbon- and nitrogen-rich phase. Further heating above 900 °C causes a strong decrease of the C:Ti and O:Ti ratios. This suggests that carbothermal reduction of the $TiO_2$ phases sets in at 900 °C. Such a reaction usually occurs above 1150 °C for bulk titanium dioxide[34] and has been recently observed at 1000 °C during the formation of TiC—carbon composites.[32]

The low reaction temperature reported herein is ascribed to the high reactivity of small intermediate $TiO_2$ nanoparticles, also seen in electron microscopy (Figure 3). SEM observations indicate that the samples are also homogeneous on the macroscopic scale (Figure S2). The anatase sample obtained at 500 °C is composed of nanoparticles of 10—20 nm diameter. (HR)TEM investigations confirm that the samples incorporate nanoparticles (Figure 3a—e) embedded within an amorphous carbon matrix. Samples obtained at 900 °C (Figure 3c) and 1000 °C (Figure 3d,e) contain Magnéli particles with a bimodal size distribution including small single-crystal nanoparticles with a diameter of 5—20 nm and 100 nm sized particles only formed at the surface. $N_2$ sorption isotherms (Figure 3f and Table S2) of the materials are of type IV, typical for mesoporous solids. Upon increasing the temperature, the BET specific surface area ($S_{BET}$) decreases from 215 $m^2 \cdot g^{-1}$ at 500 °C to 56 $m^2 \cdot g^{-1}$ at 1000 °C. Materials produced up to 900 °C exhibit small mesopores of ca. 5 nm in diameter (Figure 3g), together with bigger pores of a narrow size distribution centered at 15 nm. These textural properties reflect the structure of the carbon-rich matrix embedding the titania/Magnéli particles. This matrix also acts as a binder for the titania-Magnéli nanoparticles,[35] thus preventing strong crystalline growth up to 1000 °C and providing a medium that encapsulates and organizes nanoparticles of ca. 15 nm into a mesoporous structure. The observation of 100 nm particles indicates that extensive growth as well as sintering can occur at the surface of the calcined samples, relating to a specific reactivity at the gas flow—composite interface (Figure S3). Interestingly, sonicating a dispersion of the $Ti_8O_{15}$—carbon composite in ethanol triggers loss of the narrow mesopore size distribution while maintaining the surface area value of ca. 140 $m^2 \cdot g^{-1}$ (Figure S4). TEM observations of the sonicated sample confirm that the porous structure is broken up (Figure S4), while the nanoparticle size is unaffected, leaving the interparticle voids to be probed by $N_2$ sorption. This clearly underlines a strong mechanical contrast and weak chemical binding at the inner interfaces of the composite as well as the glassy character of the carbon phase.

The thermal stability in air of the Magnéli composites was assessed by thermogravimetric analysis (Figure S5). A mass increase between 200 and 600 °C is observed for the $Ti_4O_7$-based sample, corresponding to oxidation of the substoichiometric phase into rutile $TiO_2$.[36] The $Ti_8O_{15}$-based compound exhibits a small mass increase above 200 °C and a sharp mass drop at 450 °C. The latter is attributed to combustion of the carbon matrix. For both samples, mass spectrometry indicates that $CO_2$ and $NO_x$ are the main evolving species, whose evolution occurs between 250 and 500 °C. The final masses (103% of the initial mass for $Ti_4O_7$, 95% for $Ti_8O_{15}$) are higher than the values expected from the calculated compositions (99% and 93%, respectively). This discrepancy could originate from carbon doping into the final rutile structure, as evidenced by the yellowish hue in the oxidized samples.

Tunability of the Magnéli crystalline structure is demonstrated by modifying various parameters. The influence of the temperature on the $Ti_8O_{15}/Ti_4O_7$ phase selection was described above (Figure 2). When the calcination temperature is fixed at 900 °C, a versatile control of the composition is observed by using four different parameters (Figure 4a—d and S6), namely, (1) the titanium/polymer weight ratio, (2) the polymer chain length, (3) the polymer composition, and (4) the calcination atmosphere. The effect of each parameter is analyzed in detail in the Supporting Information. Ultimately, careful adjustment of the synthesis conditions yields pure nanocrystalline Magnéli phases: $Ti_8O_{15}$, $Ti_6O_{11}$, $Ti_5O_9$, $Ti_4O_7$, and $Ti_3O_5$ (Figure 4a—d and S6). In some cases, TiN is observed as a side product originating from nitridation either from $N_2$ atmosphere (Figure 4c, calcination of a polyethyleneglycol gel) or from nitrogen-containing organic moieties (Figure 4d, calcination of a PEI gel). Although the reaction sequence is obviously complex, some tendencies can be outlined. First, argon allows deeper reduction than the nitrogen atmosphere, suggesting that the latter is involved in a side reaction, preventing titania particles from being reduced, such as scavenging reactive species of the carbon source by evolution of $C_xN_y$ volatiles. Second, lower molecular weight, lower amounts of carbon source, and the use of PEG instead of PEI lead to stronger reduction. This could originate from different decomposition and reduction modes of the organic moieties at respectively 300 °C (evolution of alkanes and $C_xN_y$ for PEI, CO and $CO_2$ for PEG) and 900 °C. Another important parameter is the local structure of the initial hybrid gels, which involves titanium-oxo clusters and coordination bonds between the amino, oxo, or hydroxyl groups. As a control experiment, it was observed that carbothermal reduction at 900 °C under nitrogen of preformed anatase or rutile nanoparticles mixed with PEI yields Magnéli materials containing a mixture of $Ti_5O_9$ and $Ti_6O_{11}$ instead of $Ti_8O_{15}$ obtained from the homogeneous gel. This shows that phase selectivity originates from a complex interplay between the structure of the initial
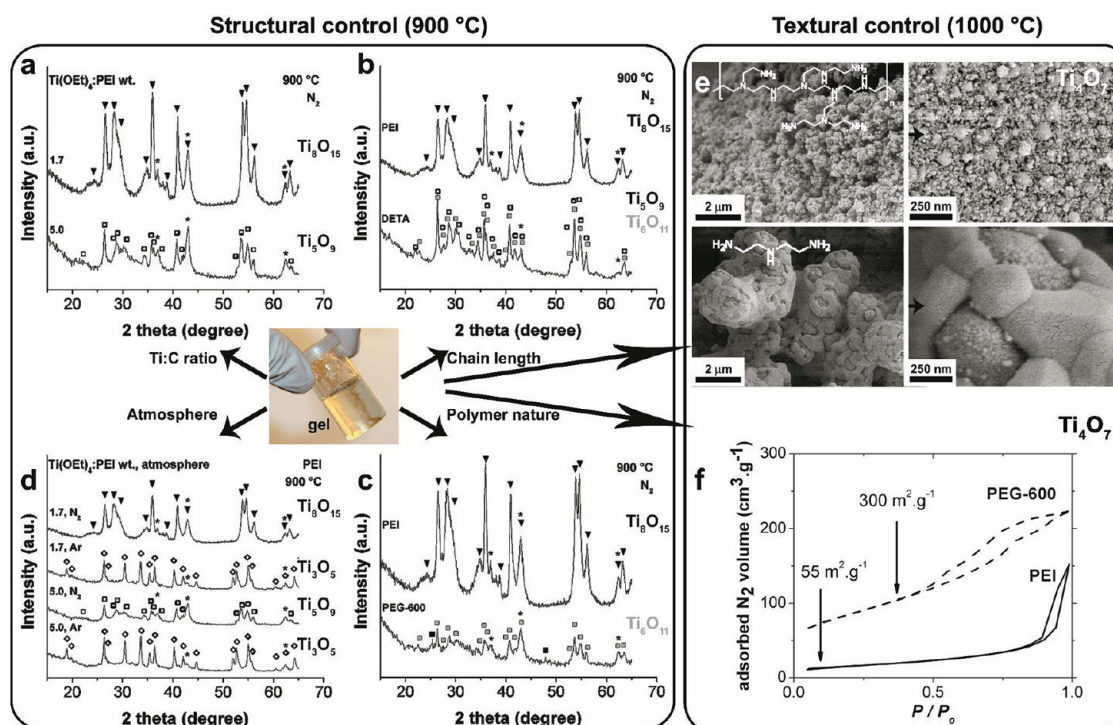
**Figure 4.** XRD investigation of the control of crystal structure and nanostructure for Magnéli phases at 900 °C: effects of (a) the Ti:C ratio, (b) the nitrogen-containing chain length, (c) the polymer nature between PEI and PEG, (d) the heating atmosphere between $N_2$ and Ar. Temperature can be used as a fifth parameter, and its effect on the phase selection is shown in Figure 2. Inversed triangles: $Ti_8O_{15}$, gray squares: $Ti_6O_{11}$, open squares: $Ti_5O_9$, open diamonds: $Ti_3O_5$, black squares: anatase $TiO_2$, stars: TiN. Textural control at 1000 °C for $Ti_4O_7$: (e) SEM images of materials originating from hybrid gels ethanol:TEOTi: PEI (top) or ethanol:TEOTi:DETA (bottom), 2:10:6 wt; (f) $N_2$ sorption isotherms of materials obtained from hybrid gels ethanol: TEOTi:PEI, 2:10:6 wt (solid line), and ethanol:TEOTi:PEG-600 (dashed line), 2:10:5.7 wt.

hybrid gels and the reactivity of the carbon matrixes in the intermediate $TiO_2-C$ composites.

Besides tuning the crystal structure, the molecular weight and the composition of the organic additive also influence the composite texture. This is exemplified by $Ti_4O_7$ composites obtained under nitrogen at 1000 °C (Figure 4e,f). By decreasing the polymer chain length from PEI to DETA while maintaining the same initial Ti:C ratio, extensive crystal growth and sintering occur (Figure 4e). Although the final carbon matrix content is the same in both cases (ca. 3 wt %), the low molecular weight of the oligomer clearly provides less efficient growth confinement infrastructure than the polymeric one. This example confirms the 3-fold role of the polymer as a reduction medium, a growth-limiting agent, and also as a porogen. On the other hand, using PEG-600 instead of PEI triggers a strong increase of the surface area of $Ti_4O_7-C$ composites with $S_{BET}$ of 300 $m^2 \cdot g^{-1}$ (Figure 4f), as compared to 55 $m^2 \cdot g^{-1}$ for PEI. Observation of the same textural properties at 900 °C (not shown) combined with the higher carbon content of PEG-based systems (17 wt % compared to 3 wt % with PEI) demonstrates the better binding of the oxo-based polymer to the particulate intermediates and the enhanced stability of the carbon matrix originating from such preorganized PEG.

The synthesis of crystalline metal oxide nanoparticles—carbon composites has been reported through hard templating[37,38] as well as soft templating.[32,39,40] While being usually less efficient in terms of accuracy of the replication, soft templating, used in our work, has the advantage of avoiding washing steps and other multiple postprocessing procedures. Moreover, the *in situ* soft templating sol—gel hybrid approach developed in this report is remarkably easier to perform and less limiting than typical three-component systems requiring a templating block copolymer, a molecular carbon source, and a titanium precursor.[32,39]

As a preliminary investigation of the impact of the phase transitions and texture variations on the electrical properties of the Magnéli phases—carbon nanocomposites, the conduction behavior of the PEI-based powders was evaluated by electrochemical impedance spectroscopy (Figure S7). The $TiO_2$-based samples behave as typical weak insulators, while Magnéli—C composites exhibit much higher conductivity. The different Magnéli materials also cover a wider range of electrical conductivity values. Indeed, the $Ti_4O_7$ composite obtained at 1000 °C is more conductive than the $Ti_8O_{15}$ sample from a 900 °C treatment. Conductivity improvement upon an increase in the processing temperature is due to three factors: (1) the crystalline phase transitions from a high band gap
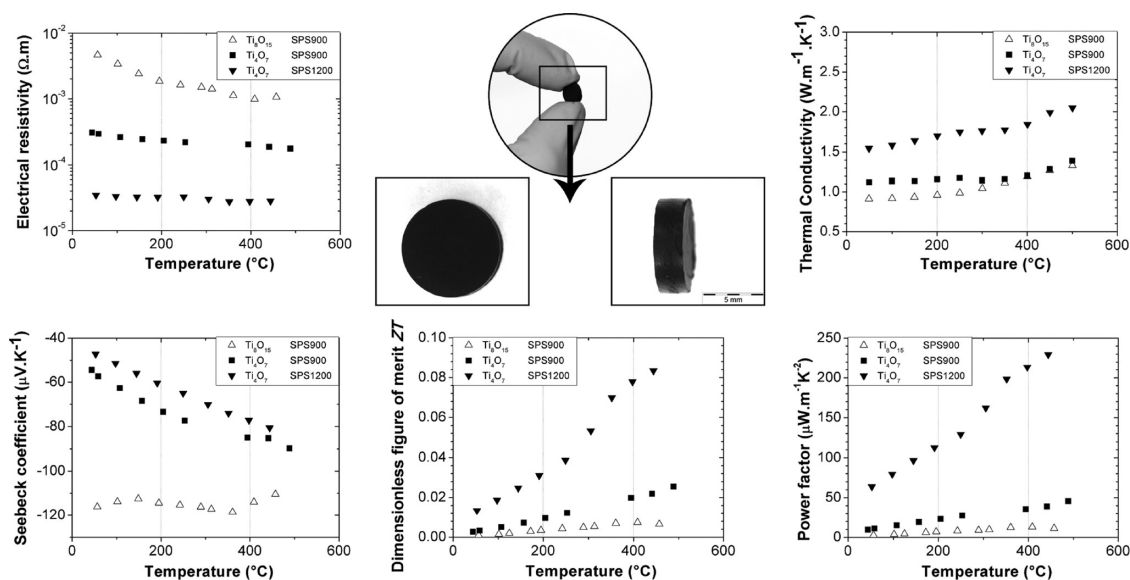
**Figure 5.** Pictures of a $Ti_4O_7$ nanocomposite monolith obtained by SPS at 900 °C. (a) Electrical resistivity, (b) thermal conductivity, (c) Seebeck coefficient, (d) thermoelectric power factor, and (e) dimensionless figure of merit for the $Ti_8O_{15}$ and $Ti_4O_7$ monoliths obtained at 900 °C.

semiconductor $TiO_2$ to the small band gap semiconductor $Ti_8O_{15}$ and to the metallic $Ti_4O_7$,[14] (2) the decrease of the porosity upon increasing the calcination temperature, and (3) the graphitization of the carbon matrix, as confirmed from Raman studies with an increase in the intensity ratio between the G band (1590 $cm^{-1}$, $E_{2g}$ vibration mode, indicative of graphitization) and the D band (1340 $cm^{-1}$, indicative of disorder) of 0.6, 0.7, and 0.9 for samples obtained respectively at 800, 900, and 1000 °C. In particular, the nanocomposites of metallic $Ti_4O_7$ with the typical high chemical stability of oxides[14] exhibit a porous structure pertinent to electrodes and a nanostructure of strong interest for thermoelectric applications.

In this regard, Harada and co-workers[3] demonstrated in their recent evaluation of the thermoelectric properties of bulk Magnéli phases that the crystallographic shear planes act as phonon-scattering centers, thus decreasing the thermal conductivity while keeping a high electron mobility. This feature is highly favorable for thermoelectric materials, whose efficiency is characterized by the dimensionless figure of merit $ZT = S^2T/\rho\kappa$, where $S$ is the Seebeck coefficient (or thermopower), $\rho$ the electrical resistivity, $\kappa$ the thermal conductivity, and $T$ the temperature. Since nanostructuring, as well as inclusion of nanopores, is a way to introduce an additional source of phonon scattering,[41] the Magnéli/carbon nanocomposites developed herein have the potential to lower the thermal conductivity while leaving other relevant quantities only weakly affected. Additionally, the high phase selectivity and texture control of the synthesis developed herein also offers the possibility to assess independently the impact of different parameters, especially the crystal phase, on the properties of the nanocomposites. In

order to produce nanostructured monoliths for the direct assessment of thermal and electrical properties or the use in a thermoelectric device, spark plasma sintering was performed at 900 °C on $Ti_8O_{15}$ nanocomposites and at 900 and 1200 °C for $Ti_4O_7$ materials, yielding centimeter-scale, stable pieces (Figures 1 and 5) with densities reaching 70% of the theoretical values of the pure bulk materials.

XRD (Figure S8) and (HR)TEM (Figure S9) confirm that the crystal structure and the size distribution of the titanium oxide particles are mostly unaffected by sintering, while only slight oxidation from $Ti_8O_{15}$ into rutile $TiO_2$ and from $Ti_4O_7$ into $Ti_5O_9$ is found by XRD. Remarkably, SPS treatment of the $Ti_4O_7$ composite at temperatures as high as 1200 °C leads to only minor changes of the crystalline species. On the other hand, SPS has an impact on the local order of carbon since graphitic domains are observed by TEM after sintering (Figure S9), which contribute to the increase in the electrical conductivity. Despite the well-known efficiency of SPS for limiting grain growth during processing of inorganic nanopowders,[42] only few examples of its application to carbon or carbon nanocomposites are reported.[28,43−45] Qi et al. showed that partial graphitization of amorphous carbon can occur during SPS, in agreement with the present results.[45] In contrast with previous results on SPS treatment of a nanoscale carbon phase with microstructured metal oxides,[28,43,44] it is shown here that SPS can be indeed favorably applied to composites of nanostructured carbon and metal oxide nanoparticles, resulting in only limited grain growth of both components and a better organized carbon phase, ultimately leading to a nanostructured conductive percolating system.

As expected, the electrical resistivity $\rho$ (Figure 5a) of the monoliths sintered at 900 °C decreases with the O/Ti ratio ($n$ decreasing), from ca. $2 \times 10^{-3}$ $\Omega \cdot m$ for $Ti_8O_{15}$ to $2 \times 10^{-4}$ $\Omega \cdot m$ for $Ti_4O_7$. These values are 1–2 orders of magnitude higher than those of the bulk suboxides.[3] $\rho$ is reduced to $3 \times 10^{-5}$ $\Omega \cdot m$ when sintering occurs at 1200 °C, which probably accounts for the graphitization of carbon, yielding conductive $Ti_4O_7$ composites. The thermal conductivity $\kappa$ below 400 °C of samples obtained at 900 °C (Figure 5b) is ca. 1 $W \cdot m^{-1} \cdot K^{-1}$, which represents an impressive reduction of ~70% with respect to the value of bulk Magnéli phases.[3,46] This is presumably due to the nanoscale interfaces that effectively scatter phonons, even at carbon contents as low as 3 wt % for samples reported herein. The thermal conductivity can be considered as the sum of a lattice contribution supported by phonons and an electronic contribution related to the electrical conductivity, $\kappa_L$ and $\kappa_e$, respectively. Nanostructuring seems to provide in this case a way to decrease the phonon component.[20,21] Additionally, the thermal conductivity below 400 °C is lower for $Ti_8O_{15}$ than $Ti_4O_7$ ($n$ decreasing), in agreement with previous results on the bulk.[3] Such a trivial comparison in the case of the bulk is made possible here for nanostructured materials only because pure suboxide phases are obtained, contrary to previously reported mixtures.[3,46] Although partial graphitization occurs at 1200 °C, growth confinement is nonetheless efficient for the corresponding $Ti_4O_7$ sample, which still exhibits a $\kappa$ reduction of 50% when compared to the bulk. The values of the Seebeck coefficient are negative (Figure 5c), indicating the n-type character of the suboxides $Ti_nO_{2n-1}$ for $n \geq 4$.[3] In agreement with previous data on the bulk,[3,46] significant variations in thermopower within the Magnéli family are observed: $S$ decreases in absolute value as $n$ decreases since $Ti_8O_{15}$ exhibits much higher absolute values of the Seebeck coefficient (ca. $-120$ $\mu V \cdot K^{-1}$ at 400 °C) than $Ti_4O_7$ ($-80$ $\mu V \cdot K^{-1}$ at 400 °C). The thermopower is not sensitive to nanostructuring since $S$ values are similar to those reported for bulk $Ti_8O_{15}$ and $Ti_4O_7$.[3] Sintering the $Ti_4O_7$ sample at 1200 °C does not significantly change $S$. Noteworthy, the temperature dependences of the thermoelectric properties of the $Ti_8O_{15}$ nanocomposite exhibit nonmonotonic variations above 400 °C, where electrical resistivity, thermal conductivity, and the Seebeck coefficient increase. Further work will be required to assess the origin of these changes, especially the behavior of the carbon subphase at such temperatures. The power factor $S^2/\rho$ at 400 °C for monoliths obtained at 900 °C is 14 and 36 $\mu W \cdot m^{-1} \cdot K^{-2}$ for $Ti_8O_{15}$ and $Ti_4O_7$, respectively. These values are lower compared to the bulk Magnéli phases[3,46] (ca. 400 $\mu W \cdot m^{-1} \cdot K^{-2}$) and account for the higher electrical resistivity of the nanocomposites. The power factor however increases strongly up to

215 $\mu W \cdot m^{-1} \cdot K^{-2}$ at 400 °C for the more conductive sample sintered at 1200 °C. For the same sintering temperature (900 °C), $Ti_8O_{15}$ exhibits a lower dimensionless figure of merit $ZT$ than $Ti_4O_7$ (Figure 5e). This trend contradicts results on bulk phases, for which $ZT$ increases as $n$ increases and is ascribed to the poor electrical conductivity of the $Ti_8O_{15}$ sample.[3] Despite the lower thermal conductivity for the composites than for bulk compounds, samples obtained at 900 °C show lower $ZT$ at 400 °C ($8 \times 10^{-3}$ and $2 \times 10^{-2}$ for $Ti_8O_{15}$ and $Ti_4O_7$, respectively) than bulk phases (0.10 and 0.07 for $Ti_8O_{15}$ and $Ti_4O_7$, respectively,[3] ca. 0.1 for mixtures of Magnéli phases[3,46]). This limitation is mainly attributed to the poor electron conduction in the carbon phase and can be overcome by partial graphitization by SPS at 1200 °C. Indeed, $ZT$ values are then boosted up to ca. 0.08 at 400 °C for $Ti_4O_7$. Now, the "nano-Magnéli" $Ti_4O_7$-based composite reaches a $ZT$ higher than its bulk counterpart (0.07 for the same phase $Ti_4O_7$)[3] and close to those reported for other Magnéli phases (ca. 0.1 for $Ti_8O_{15}$[3] and mixtures[3,46]).

It is clear that the present system shows just the potential of a combined sol−gel/SPS strategy to develop innovative thermoelectric materials and that further optimizations of the texture, the electronic interface coupling, and the structure of the carbon subphase are nevertheless required to reach the best performances reported for n-type metal oxides.[29,30,46,47] In particular, these results show that potential candidates for thermoelectric materials can be found within the combination of nanoscale oxides with intrinsically high thermoelectric efficiency (low $\rho$, low $\kappa$, and high $S$) with a conductive carbon phase as a binder and interface modifier. The results described above for the sample treated at 1200 °C indicate that, although the electrical conductivity might suffer from the incorporation of nanostructured carbon, the associated strong reduction of thermal conductivity can be sufficient to overcome this drawback and to provide overall comparable, if not better, performances than bulk compounds. One way of improving thermoelectric performances in these systems may be based on an increase in the electrical conductivity of the carbon component. This can be achieved by reaching higher graphitic order through refinement of the polymeric carbon precursor and/or introduction of small amounts of catalysts. These routes are currently under investigation in our groups. Another key factor is further probing and refining of the metal oxide/carbon heterojunction, as interfacial effects are known to be able to improve charge separation and to boost electrical conductivity of hybrids and composites.[48]

## CONCLUSIONS

To conclude, the hybrid materials chemistry strategy developed in this study combines the typical versatility

of the sol−gel process with SPS, a technique that is still in its infancy when considering the potential of this rapid method, which maintains nanoscale features. Both processes provide their own advantages, namely, adaptability, scalability, and low cost of the sol−gel process and fast and growth-limiting sintering for SPS. We show that SPS is suitable to sinter intimate mixtures of nanostructured carbon and metal oxide nanoparticles originating from a one-pot sol−gel process. The efficiency and novelty of this combined approach are demonstrated by the nature of the obtained metal oxide nanocrystals: most of the Magnéli phases described above are obtained for the first time as single nanocrystalline phases. Additionally, we demonstrate that increased thermoelectric conversion efficiency *via*

reduction of the thermal conductivity of the n-type Magnéli/carbon nanocomposites is achievable. This suggests that more efficient materials, with high electron conduction, could be designed through this approach, which might position them favorably as cheap, stable, and sustainable materials for a real large-scale, societal application of thermoelectricity. We expect that the simplicity of the "one-pot" sol−gel step proposed herein will stimulate intensive research in the chemistry and physics as well as on potential application of Magnéli nanophases. Intense, further extension of this method to other binary and ternary metal oxides should certainly pave the way toward innovative advanced materials for energy harvesting and optoelectronics.

## METHODS

**Hybrid Gel Preparation.** Hybrid gels were prepared by mixing ethanol, titanium tetraethoxide (TEOTi), and various carbon/nitrogen sources. C/N-source polymer-based gels were prepared according to the following typical procedure: various amounts (2.0 to 6.0 g) of branched poly(ethyleneimine) (25 000 g·mol$^{-1}$) were mixed with 2.0 g of ethanol and 10.0 g of titanium(IV) ethoxide. The opaque mixtures were stirred overnight at 80 °C and then heated at 100 °C for 2 h to obtain limpid yellow gels. A C/N-source oligomer-based gel was obtained by mixing 6.0 g of diethylenetriamine with 2.0 g of ethanol and 10.0 g of titanium(IV) ethoxide. The mixture was stirred at 90 °C for 1 h to obtain a limpid gel. A C/O-source polymer-based gel was formed by mixing 6.3 g of polyethyleneglycol (600 g·mol$^{-1}$, PEG-600) with 2.0 g of ethanol and 10.0 g of titanium(IV) ethoxide. The mixtures were stirred overnight at 60 °C for 1 h to obtain a limpid gel.

**Calcination Procedure.** The hybrid gels were placed in a crucible, maintained at room temperature under nitrogen flow for 1 h, heated at 5 °C·min$^{-1}$, and then maintained at a temperature between 500 and 1000 °C for 4 h.

**Spark Plasma Sintering and Shaping of the Monoliths.** The finely ground powders were compacted by spark plasma sintering (Dr. Sinter 5155, Synthex Ltd., Tokyo, Japan). Around 270 mg of powders was wrapped in Ta foil and densified using carbon dyes under a pressure of *ca.* 60 MPa. The samples were heated to 900 °C (or 1200 °C) with a heating rate of 200 °C·min$^{-1}$ and directly cooled to room temperature. For measurement of the transport properties, the samples were cut with a diamond wire saw into specimens of typical dimensions 1.5 × 1.5 × 8 mm³.

**Characterization.** XRD was performed on a D8 Bruker powder diffractometer operating at Cu-Kα1 radiation. Carbon, hydrogen, and nitrogen contents were measured using a Vario EL Elementar instrument. The Ti content was estimated at the Fraunhofer Institute für Angewandte Polymerforschung, Golm, using ICP-OES. The O content was obtained by subtraction. TGA was performed on a TG 209 F1 Netzsch apparatus under nitrogen or synthetic air flow of 15 mL·min$^{-1}$, with a 10 °C·min$^{-1}$ heating rate. Prior to N$_2$ sorption measurements, samples were degassed at 150 °C for 20 h. After measurement on a Quadrasorb apparatus at 77 K, specific surface areas and pore size distributions were evaluated by the BET and BJH methods, respectively. Scanning electron microscopy was performed on a LEO 1550- Gemini instrument. The samples were loaded on carbon-coated stubs and coated by sputtering an Au/Pd alloy prior to imaging. TEM studies were carried out by using a Philips CM 200 (LaB$_6$ cathode) apparatus. Samples were prepared by dipping a carbon-coated copper grid into the finely ground powders or by evaporating a drop of diluted

suspension in ethanol on the grid. Raman spectra were recorded on a WiTec confocal Raman microscope, alpha300 R, with a Nd/YAG laser wavelength of 532 nm. Electrochemical impedance spectroscopy (EIS) was performed in a three-electrode cell using a Pt counter electrode, a Ag/AgCl reference electrode, and a working electrode built from a sample pellet obtained at 12 T·cm$^{-2}$ in contact with a glassy carbon electrode. The electrolyte was H$_2$SO$_4$, 0.5 mol·L$^{-1}$. A Gamry Reference 600 potentiostat was used to record the EIS spectra between 10$^6$ and 0.01 Hz at a voltage of 0.6 V with a peak to peak perturbation of 20 mV. Experiments were repeated three times on the same working electrodes as well as on different electrodes to check the reproducibility of the collected data. The electrochemical response at high frequency, resembling a partial semicircle, was fitted according to a model circuit incorporating a resistance accounting for the electrolyte behavior in series with a circuit modeling the electrode, made of a resistance in parallel with a constant phase element accounting for the double layer capacitance and the porosity of the electrode. An additional setup consisting in a solid cell containing the pressed powders (30 mg) confined between two blocking Pt electrodes was used with a Gamry Reference 600 low-impedance cable to reduce the mutual inductive effect and provide qualitative measurement of the sample conductivity. The electrical resistivity and Seebeck coefficient were measured simultaneously in the temperature range from 300 to 750 K using a ZEM-3 instrument (ULVAC-RIKO). The thermal diffusivity $\lambda$ was determined in the temperature range from 300 to 750 K using the laser flash technique (LFA 447 Micro Flash, Netzsch). The thermal conductivity $\kappa$ was derived from the relationship $\kappa \approx C_p d\lambda$, where *d* is the sample density and $C_p$ is the specific heat. As a first approximation, the former was considered constant in the temperature range investigated, while the latter was estimated according to a linear fit of the $C_p$ values reported by Lakkis *et al.* in the range 370−450 K for bulk Ti$_4$O$_7$.[49]

*Supporting Information Available:* Reference XRD patterns of titania/Magnéli phases, composition and textural features of as-obtained titania/Magnéli-based composites, and

thermogravimetric analysis under nitrogen of an initial hybrid gel. SEM images of as-obtained titania/Magnéli composites, SEM picture of the surface of a $Ti_8O_{15}$ composite, $N_2$ sorption isotherms and TEM pictures of a $Ti_8O_{15}$ composite before and after sonication in ethanol and drying, and TGA traces under air of $Ti_8O_{15}$ and $Ti_4O_7$ composites obtained from PEI gels. Detailed discussion of the control of Magnéli structures at 900 °C and of the control of the texture at 1000 °C for $Ti_4O_7$, and electrochemical impedance spectra in the Nyquist plane of $TiO_2$ and $Ti_4O_7$ composites. Conductance evolution *versus* the calcination temperature, XRD patterns of $Ti_8O_{15}$ and $Ti_4O_7$ samples before and after SPS processing at 900 and 1200 °C, respectively, and (HR)TEM pictures of a $Ti_4O_7$ sample processed by SPS at 900 °C. This material is available free of charge *via* the Internet at http://pubs.acs.org.

## REFERENCES AND NOTES

1. Kwon, D.-H.; Kim, K. M.; Jang, J. H.; Jeon, J. M.; Lee, M. H.; Kim, G. H.; Li, X.-S.; Park, G.-S.; Lee, B.; Han, S.; *et al.* Atomic Structure of Conducting Nnanofilaments in $TiO_2$ Resistive Switching Memory. *Nat. Nanotechnol.* **2010**, *5*, 148–153.

2. Ohkoshi, S.-i.; Tsunobuchi, Y.; Matsuda, T.; Hashimoto, K.; Namai, A.; Hakoe, F.; Tokoro, H. Synthesis of a Metal Oxide with a Room-Temperature Photoreversible Phase Transition. *Nat. Chem.* **2010**, *2*, 539–545.

3. Harada, S.; Tanaka, K.; Inui, H. Thermoelectric Properties and Crystallographic Shear Structures in Titanium Oxides of the Magnèli Phases. *J. Appl. Phys.* **2010**, *108*, 083703–6.

4. Andersson, S.; Collén, B.; Kruuse, G.; Kuylenstierna, U.; Magnéli, A.; Pestmalis, H.; Åsbrink, S. Identification of Titanium Oxides by X-ray Powder Patterns. *Acta Chem. Scand.* **1957**, *11*, 1653–1657.

5. Andersson, S.; Collén, B.; Kuylenstierna, U.; Magnéli, A. Phase Analysis Studies on the Titanium-Oxygen System. *Acta Chem. Scand.* **1957**, *11*, 1641–1652.

6. Asbrink, S.; Magnéli, A. Crystal Structure Studies on Trititanium Pentoxide $Ti_3O_5$. *Acta Chem. Scand.* **1959**, *12*, 575–581.

7. Andersson, S. The Crystal Structure of $Ti_5O_9$. *Acta Chem. Scand.* **1960**, *14*, 1161–1172.

8. Le Page, Y.; Strobel, P. Structural Chemistry of Magnéli Phases $Ti_nO_{2n-1}$ ($4 \leq n \leq 9$). I. Cell and Structure Comparisons. *J. Solid State Chem.* **1982**, *43*, 314–319.

9. Le Page, Y.; Strobel, P. Structural Chemistry of the Magnéli Phases $Ti_nO_{2n-1}$, $4 \leq n \leq 9$: II. Refinements and Structural Discussion. *J. Solid State Chem.* **1982**, *44*, 273–281.

10. Le Page, Y.; Strobel, P. Structural Chemistry of Magnéli Phases $Ti_nO_{2n-1}$ ($4 \leq n \leq 9$). III. Valence Ordering of Titanium in $Ti_6O_{11}$ at 130 K. *J. Solid State Chem.* **1983**, *47*, 6–15.

11. Le Page, Y.; Marezio, M. Structural Chemistry of Magnéli Phases $Ti_nO_{2n-1}$ ($4 \leq n \leq 9$): IV. Superstructure in $Ti_4O_7$ at 40 K. *J. Solid State Chem.* **1984**, *53*, 13–21.

12. Bartholomew, R. F.; Frankl, D. R. Electrical Properties of Some Titanium Oxides. *Phys. Rev.* **1969**, *187*, 828.

13. Hayfield, P. C. S. Electrode Materials, Electrode and Electrochemical Cells. U.S. patent 4422917, 1983.

14. Smith, J. R.; Walsh, F. C.; Clarke, R. L. Electrodes Based on Magnéli Phase Titanium Oxides: the Properties and Applications of Ebonex® Materials. *J. Appl. Electrochem.* **1998**, *28*, 1021–1033.

15. Siracusano, S.; Baglio, V.; D'Urso, C.; Antonucci, V.; Aricò, A. S. Preparation and Characterization of Titanium Suboxides as Conductive Supports of $IrO_2$ Electrocatalysts for Application in SPE Electrolysers. *Electrochim. Acta* **2009**, *54*, 6292–6299.

16. Clarke, R. L. Conductive Titanium Suboxide Particulates. U.S. patent 5173215, 1992.

17. James, D.; Allison, D. B., II; Kelley, J. J.; Doe, J. B. Electrical Energy Devices. U.S. patent 2003/0036001 A1, 2003.

18. Ellis, K.; Hill, A.; Hill, J.; Loyns, A.; Partington, T. The Performance of Ebonex® Electrodes in Bipolar Lead-Acid Batteries. *J. Power Sources* **2004**, *136*, 366–371.

19. Bejan, D.; Malcolm, J. D.; Morrison, L.; Bunce, N. J. Mechanistic Investigation of the Conductive Ceramic Ebonex® as an Anode Material. *Electrochim. Acta* **2009**, *54*, 5548–5556.

20. Yu, C.; Kim, Y. S.; Kim, D.; Grunlan, J. C. Thermoelectric Behavior of Segregated-Network Polymer Nanocomposites. *Nano Lett.* **2008**, *8*, 4428–4432.

21. See, K. C.; Feser, J. P.; Chen, C. E.; Majumdar, A.; Urban, J. J.; Segalman, R. A. Water-Processable Polymer−Nanocrystal Hybrids for Thermoelectrics. *Nano Lett.* **2010**, *10*, 4664–4667.

22. Mercier, J.; Lakkis, S. Preparation of Titanium Lower Oxides Single Crystals by Chemical Transport Reaction. *J. Cryst. Growth* **1973**, *20*, 195–201.

23. Strobel, P.; Le Page, Y. Growth of $Ti_8O_{17}$ Crystals by Chemical Vapor Transport. *J. Cryst. Growth* **1982**, *56*, 723–726.

24. Strobel, P.; Page, Y. Crystal Growth of $Ti_nO_{2n-1}$ Oxides ($n$=2 to 9). *J. Mater. Sci.* **1982**, *17*, 2424–2430.

25. Afir, A.; Achour, M.; Saoula, N. X-ray Diffraction Study of Ti-O-C System at High Temperature and in a Continuous Vacuum. *J. Alloys Compd.* **1999**, *288*, 124–140.

26. Gusev, A. A.; Avvakumov, E. G.; Medvedev, A. Z.; Masliy, A. I. Ceramic Electrodes Based on Magneli Phases of Titanium Oxides. *Sci. Sintering* **2007**, *39*, 51–57.

27. Han, W.-Q.; Zhang, Y. Magnéli Phases $Ti_nO_{2n-1}$ Nanowires: Formation, Optical, and Transport Properties. *Appl. Phys. Lett.* **2008**, *92*, 203117–203119.

28. Mo, C. B.; Cha, S. I.; Kim, K. T.; Lee, K. H.; Hong, S. H. Fabrication of Carbon Nanotube Reinforced Alumina Matrix Nanocomposite by Sol-Gel Process. *Mater. Sci. Eng., A* **2005**, *395*, 124–128.

29. Ohta, S.; Ohta, H.; Koumoto, K. Grain Size Dependence of Thermoelectric Performance of Nb-Doped $SrTiO_3$ Polycrystals. *J. Ceram. Soc. Jap.* **2006**, *114*, 102–105.

30. Ohtaki, M.; Araki, K.; Yamamoto, K. High Thermoelectric Performance of Dually Doped ZnO Ceramics. *J. Electron. Mater.* **2009**, *38*, 1234–1238.

31. Hirasawa, M.; Seto, T.; Orii, T.; Aya, N.; Shimura, H. Synthesis of Size-Selected $TiO_x$ Nanoparticles. *Appl. Surf. Sci.* **2002**, *197−198*, 661–665.

32. Huang, C.-H.; Gu, D.; Zhao, D.; Doong, R.-A. Direct Synthesis of Controllable Microstructures of Thermally Stable and Ordered Mesoporous Crystalline Titanium Oxides and Carbide/Carbon Composites. *Chem. Mater.* **2010**, *22*, 1760–1767.

33. Wahlbeck, P. G.; Gilles, P. W. Reinvestigation of the Phase Diagram for the System Titanium-Oxygen. *J. Am. Ceram. Soc.* **1966**, *49*, 180–183.

34. White, G. V.; Mackenzie, K. J. D.; Brown, I. W. M.; Bowden, M. E.; Johnston, J. H. Carbothermal Synthesis of Titanium Nitride. *J. Mater. Sci.* **1992**, *27*, 4294–4299.

35. Li, D.; Zhou, H.; Honma, I. Design and Synthesis of Self-Ordered Mesoporous Nanocomposite Through Controlled *in-situ* Crystallization. *Nat. Mater.* **2004**, *3*, 65–72.

36. Chen, G.; Bare, S. R.; Mallouk, T. E. Development of Supported Bifunctional Electrocatalysts for Unitized Regenerative Fuel Cells. *J. Electrochem. Soc.* **2002**, *149*, A1092–A1099.

37. Fischer, A.; Jun, Y.-S.; Thomas, A.; Antonietti, M. Synthesis of High-Surface-Area TiN/Carbon Composite Materials with Hierarchical Porosity *via* Reactive Templating. *Chem. Mater.* **2008**, *20*, 7383–7389.

38. Jun, Y.-S.; Hong, W. H.; Antonietti, M.; Thomas, A. Mesoporous, 2D Hexagonal Carbon Nitride and Titanium Nitride/Carbon Composites. *Adv. Mater.* **2009**, *21*, 4270–4274.

39. Yu, T.; Deng, Y.; Wang, L.; Zhang, L.; Tu, B.; Zhao, D. Ordered Mesoporous Nanocrystalline Titanium-Carbide/Carbon Composites from *in situ* Carbothermal Reduction. *Adv. Mater.* **2007**, *19*, 2301–2306.

40. Stefik, M.; Lee, J.; Wiesner, U. Nanostructured Carbon-Crystalline Titania Composites from Microphase Separation of Poly(ethylene oxide-b-acrylonitrile) and Titania Sols. *Chem. Commun.* **2009**, 2532–2534.

41. Harman, T. C.; Taylor, P. J.; Walsh, M. P.; LaForge, B. E. Quantum Dot Superlattice Thermoelectric Materials and Devices. *Science* **2002**, *297*, 2229–2232.

42. Munir, Z.; Anselmi-Tamburini, U.; Ohyanagi, M. The Effect of Electric Field and Pressure on the Synthesis and Consolidation of Materials: A Review of the Spark Plasma Sintering Method. *J. Mater. Sci.* **2006**, *41*, 763–777.

43. Dusza, J.; Blugan, G.; Morgiel, J.; Kuebler, J.; Inam, F.; Peijs, T.; Reece, M. J.; Puchy, V.; Pressed, Hot and Spark Plasma Sintered Zirconia/Carbon Nanofiber Composites. *J. Eur. Ceram. Soc.* **2009**, *29*, 3177–3184.

44. Wu, Y. J.; Su, S. H.; Cheng, J. P.; Chen, X. M. Spark Plasma Sintering of Barium Zirconate Titanate/Carbon Nanotube Composites with Colossal Dielectric Constant and Low Dielectric Loss. *J. Am. Ceram. Soc.* **2011**, *94*, 663–665.

45. Qi, X.; Bao, Q.; Li, C. M.; Gan, Y.; Song, Q.; Pan, C.; Tang, D. Y. Spark Plasma Sintering-Fabricated One-Dimensional Nanoscale "Crystalline-Amorphous" Carbon Heterojunction. *Appl. Phys. Lett.* **2008**, *92*, 113113–113115.

46. He, Q.; Hao, Q.; Chen, G.; Poudel, B.; Wang, X.; Wang, D.; Ren, Z. Thermoelectric Property Studies on Bulk $TiO_x$ with $x$ from 1 to 2. *Appl. Phys. Lett.* **2007**, *91*, 052505.

47. Berardan, D.; Guilmeau, E.; Maignan, A.; Raveau, B. $In_2O_3$: Ge, a Promising n-Type Thermoelectric Oxide Composite. *Solid State Commun.* **2008**, *146*, 97–101.

48. Maier, J.; Nanoionics, Ion Transport and Electrochemical Storage in Confined Systems. *Nat. Mater.* **2005**, *4*, 805–815.

49. Lakkis, S.; Schlenker, C.; Chakraverty, B. K.; Buder, R.; Marezio, M. Metal-Insulator Transitions in $Ti_4O_7$ Single Crystals: Crystal Characterization, Specific Heat, and Electron Paramagnetic Resonance. *Phys. Rev. B* **1976**, *14*, 1429.